Phase-stabilized two-dimensional electronic spectroscopy

Tobias Brixner, Tomáš Manal, Igor V. Stiopkin, and Graham R. Fleming

Citation: The Journal of Chemical Physics **121**, 4221 (2004); doi: 10.1063/1.1776112
View online: http://dx.doi.org/10.1063/1.1776112
View Table of Contents: http://scitation.aip.org/content/aip/journal/jcp/121/9?ver=pdfcov
Published by the AIP Publishing

Phase-stabilized two-dimensional electronic spectroscopy

Tobias Brixner, Tomáš Mančal, Igor V. Stiopkin, and Graham R. Fleming[a)]
Department of Chemistry, University of California, Berkeley and Physical Biosciences Division, Lawrence Berkeley National Laboratory, Berkeley, California 94720

(Received 15 April 2004; accepted 4 June 2004)

Two-dimensional (2D) spectroscopy is a powerful technique to study nuclear and electronic correlations between different transitions or initial and final states. Here we describe in detail our development of inherently phase-stabilized 2D Fourier-transform spectroscopy for electronic transitions. A diffractive-optic setup is used to realize heterodyne-detected femtosecond four-wave mixing in a phase-matched box geometry. Wavelength tunability in the visible range is accomplished by means of a 3 kHz repetition-rate laser system and optical parametric amplification. Nonlinear signals are fully characterized by spectral interferometry. Starting from fundamental principles, we discuss the origin of phase stability and the precise calibration of excitation-pulse time delays using movable glass wedges. Automated subtraction of undesired scattering terms removes experimental artifacts. On the theoretical side, the response-function formalism is extended to describe molecules with three electronic levels, and the shape of 2D spectral features is discussed. As an example for this technique, experimental 2D spectra are shown for the dye molecule Nile Blue in acetonitrile at 595 nm, recorded for a series of population times. Simulations explore the influence of different model parameters and qualitatively reproduce the experimental results. We show that correlations between different electronically excited states can be determined from the spectra. The technique described here can be used to measure the third-order response function of complex systems covering several electronic transitions. © *2004 American Institute of Physics.* [DOI: 10.1063/1.1776112]

I. INTRODUCTION

Ultrafast spectroscopy is increasingly employed for the study of condensed-phase systems which cannot be characterized by a single two-level electronic or vibrational system coupled to a bath. Sophisticated methods have been developed to explore the underlying microscopic dynamics and to disentangle the interaction of multiple chromophores. Especially the techniques of multidimensional femtosecond spectroscopy are suitable to investigate electronic and vibrational couplings. Theoretical discussions have been given by Mukamel *et al.*[1–3] and Cho.[4] Pioneering experiments as well as simulations have been reported for vibrational transitions by Hamm *et al.* using dynamic hole burning,[5,6] and from the groups of Hochstrasser[7–9] and Tokmakoff[10–12] using heterodyne-detected photon echoes. Heterodyne detection of nonlinear signals was furthermore discussed by Joffre *et al.*[13–15] and Wiersma *et al.*,[16] and two-dimensional spectroscopy of electronic transitions was introduced and described in great detail by Jonas and co-workers[17–21] who also reviewed the subject recently.[22] In these experiments, phase-matched four-wave mixing (FWM) signals are analyzed by some version of heterodyne detection in order to obtain information about both amplitude and phase of the nonlinear third-order signal. Fourier evaluation then leads to two-dimensional (2D) spectra which can be intuitively interpreted and can be seen as an extension of spectrally resolved pump probe where an additional coordinate describes the dependence of the transient spectra on the excitation frequency. An approach to 2D spectroscopy with femtosecond pulse-shaping techniques was recently presented by Warren and coworkers.[23] Time-domain heterodyne techniques to fully characterize nonlinear signals have also been discussed,[24–27] but because of the need to scan an additional time delay they are more difficult to implement than frequency-dependent techniques.

Until recently, 2D electronic spectroscopy has been limited to the wavelength range provided by the very stable output of Ti:sapphire oscillators.[22] In order to observe a larger range of electronic transitions throughout the visible spectral region, it was desirable to develop methods suitable for broadly tunable light sources such as optical parametric amplifiers (OPA). There, the required interferometric phase stability and positioning accuracy of pulse time delays is more difficult to achieve than for the near-infrared or mid-infrared regime: For shorter wavelengths, path-length and Poynting fluctuations lead to correspondingly larger phase errors. In related applications, passive phase stabilization was achieved by use of diffractive optics (DO),[28–32] and Miller *et al.* also reported preliminary heterodyne-detected photon echoes using DO.[33] We have recently reported full 2D traces recorded in our development of frequency-tunable noncollinear DO-based FWM with heterodyne detection of three-pulse photon echoes by spectral interferometry, in short, 2D Fourier spectrometry for the visible region.[34] Very accurate pulse delays are provided by movable glass wedges. Two-dimensional spectra were also obtained by Miller *et al.*[35] in their related but different geometrical setup.

a)Electronic mail: grfleming@lbl.gov

In this paper we describe in detail the experimental technique and the theoretical treatment of 2D phase-stabilized spectroscopy in the visible, and illustrate these issues on a prototypical dye molecule. The organization of the manuscript is as follows: In Sec. II, the principle of 2D spectroscopy is briefly reviewed, forming the basis for the following discussions. The experimental technique is presented in Sec. III, focusing on the DO-based setup and its role in phase stabilization (Sec. III A), the accurate calibration of time delays (Sec. III B), the data acquisition and evaluation procedure including the subtraction of unwanted scattering terms (Sec. III C), and the subject of absolute-phase determination (Sec. III D). In Sec. IV, the theory for 2D spectroscopy involving more than two electronic states is developed. A discussion of results is given in Sec. V. Experimental 2D traces (Sec. V A) are reported for Nile Blue in acetonitrile at 595 nm, and the simulations (Sec. V B) indicate general dependencies of these spectra on model parameters. Conclusions are given in Sec. VI, and the Appendix contains the derivation of the three-level response function.

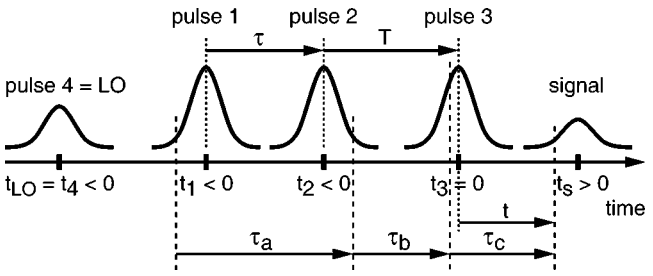

FIG. 1. Definition of time variables. Time zero is defined at the center of the third excitation pulse. The first two excitation pulses arrive at times $t_1<0$ and $t_2<0$, separated by the coherence time τ which is positive for the shown pulse order, and negative if pulse 2 arrives first. The population time $T>0$ is the separation between the second and third excitation pulse at $t_3=0$. Nonlinear third-order polarization at time t is induced by field interactions at times $\tau_a+\tau_b+\tau_c$, $\tau_b+\tau_c$, and τ_c earlier, which may occur somewhere under the excitation pulse envelopes. This leads to a free-induction decay and for inhomogeneously broadened systems, an additional photon echo signal is observed with an average arrival time t_s that is similar to the coherence time. The local oscillator (LO) used for heterodyned signal detection always arrives first at time t_4.

II. PRINCIPLE OF TWO-DIMENSIONAL SPECTROSCOPY

Two-dimensional femtosecond spectroscopy aims at determining the complete third-order optical response function of quantum-mechanical systems such as molecules or aggregates. For this purpose, a sequence of three ultrashort laser pulses is used to excite the sample, and the emitted signal field is characterized in amplitude and phase as a function of frequency and as a function of the excitation-pulse time delays. After suitable data analysis involving Fourier-transform methods, one obtains two-dimensional frequency "maps" of the system's behavior. Two-dimensional spectroscopy has been reviewed in detail elsewhere.[22] Here we restrict ourselves to the basic formalism that will be used in later sections.

Perturbation theory can be used to calculate the third-order polarization

$$P^{(3)}(t)=\int_0^\infty\int_0^\infty\int_0^\infty S^{(3)}(\tau_a,\tau_b,\tau_c)E(t-\tau_a-\tau_b-\tau_c)\times E(t-\tau_b-\tau_c)E(t-\tau_c)d\tau_a d\tau_b d\tau_c, \quad (1)$$

at time t and one specific point in space, induced by three electric-field interactions in the past at times $t-\tau_a-\tau_b-\tau_c$, $t-\tau_b-\tau_c$, and $t-\tau_c$ (see Fig. 1 for a definition of time variables). The real-valued third-order time-domain response function $S^{(3)}(\tau_a,\tau_b,\tau_c)$ is hence given as the polarization excited by three δ-function pulses. The response function is nonzero only for τ_a, τ_b, and $\tau_c>0$ to ensure causality.

Inverse Fourier transformation of $S^{(3)}(\tau_a,\tau_b,\tau_c)$ with respect to the interaction times then leads to the complex-valued third-order frequency-domain susceptibility $\chi^{(3)}(\omega_a,\omega_b,\omega_c)$. For an experimental determination of S or χ one therefore needs to vary the interaction times in a systematic fashion. However, it needs to be considered that, since time-domain electric fields are real-valued quantities, the frequency-domain electric fields are complex and contribute to χ with positive as well as negative frequencies.

In a noncollinear geometry, it is possible to use phase matching to select the signs of the frequencies contributing to the observed signal because different sign combinations lead to signal radiation into different spatial directions.[22] For example, with the noncollinear box geometry employed below (compare Fig. 2), we detect the signal along wave-vector direction $\vec{k}_s=-\vec{k}_1+\vec{k}_2+\vec{k}_3$, where $\vec{k}_1$, $\vec{k}_2$, and $\vec{k}_3$ are the wave vectors of the three excitation pulses with frequencies ω_1, ω_2, and ω_3. Hence the polarization has contributions for negative ω_1, positive ω_2, and positive ω_3. Since the pulses have finite durations, however, the interactions in Eq. (1) can occur in any order and also at any time under the pulse envelopes. It is therefore not possible to vary τ_a, τ_b, and τ_c directly, but only the pulse centers at t_1, t_2, and t_3. The (real-valued) temporal electric field interacting with the sample can then be described as

$$E(t)=\tilde{A}(t-t_1)e^{-i\omega_0(t-t_1)+i\vec{k}_1\cdot\vec{r}}+\tilde{A}(t-t_2)\times e^{-i\omega_0(t-t_2)+i\vec{k}_2\cdot\vec{r}}+\tilde{A}(t-t_3)e^{-i\omega_0(t-t_3)+i\vec{k}_3\cdot\vec{r}}+\text{c.c.}, \quad (2)$$

with carrier frequency (i.e., central laser frequency) ω_0, complex envelopes $\tilde{A}(t')=A(t')\exp[-i\varphi(t')]$, and c.c. denoting the complex conjugate of all previous expressions. The complex envelope contains both the shape [e.g., a Gaussian $A(t')=\exp[-2\ln 2(t'/\tau_p)^2]$ with intensity-full width at half maximum (FWHM) pulse duration τ_p] as well as any phase modulation $\varphi(t')$. Note that the time shifts t_i should be contained in both the envelopes as well as in the oscillatory phase terms.[36,37] Time zero is set at the center of the third pulse, i.e., $t_3=0$. It is customary to define the coherence time τ as the separation between the centers of the first two pulses, $\tau=t_2-t_1$, and the population time T as the difference between the second and third pulse, $T=-t_2$ for the pulse order shown in Fig. 1.

The multiplication $E(t-\tau_a-\tau_b-\tau_c)E(t-\tau_b-\tau_c)E(t-\tau_c)$ in Eq. (1) using the field of Eq. (2) yields $6\times6\times6=216$ terms of the form of multiplication of three envelope functions $\tilde{A}(t)$ or $\tilde{A}^*(t)$ and corresponding phase factors determining their directions and frequencies. Each term of this sum corresponds to a specific time order of interaction contributions. For example, the contribution

$$\begin{aligned}&\tilde{A}(t-t_2-\tau_a-\tau_b-\tau_c)\tilde{A}^*(t-t_1-\tau_b-\tau_c)\\&\quad\times\tilde{A}(t-t_3-\tau_c)e^{-i\omega_0(t-t_2-\tau_a-\tau_b-\tau_c)}\\&\quad\times e^{i\omega_0(t-t_1-\tau_b-\tau_c)}e^{-i\omega_0(t-t_3-\tau_c)}e^{i(\vec{k}_2-\vec{k}_1+\vec{k}_3)\cdot\vec{r}},\end{aligned}\tag{3}$$

corresponds to the case when the system first interacts with the pulse going along the $\vec{k}_2$ direction at the time $t-\tau_a-\tau_b-\tau_c$, then it interacts with the pulse characterized by the direction $-\vec{k}_1$ at time $t-\tau_b-\tau_c$ and finally with the pulse traveling along $\vec{k}_3$ at time $t-\tau_c$. The star denotes complex conjugation. Only six of the 216 terms generate a signal in the direction of $-\vec{k}_1+\vec{k}_2+\vec{k}_3$ along which we measure. All terms possess a common phase factor $e^{-i\omega_0 t+i\omega_0\tau}$, and in addition they contain one of the phase factors that can be either $e^{i\omega_0(\tau_a+\tau_c)}$, $e^{-i\omega_0(\tau_c-\tau_a)}$, or $e^{i\omega_0(\tau_a+2\tau_b+\tau_c)}$.

Depending on the system in question, the response function $S^{(3)}(\tau_a,\tau_b,\tau_c)$ contains a sum of contributions with similar phase factors. If the laser frequency ω_0 approximately matches the electronic transition frequencies in the system, some of the phase factors originating from the response function may cancel with those originating from the laser field. Thus, under the integration in Eq. (1) we would have slowly varying terms (where oscillatory factors canceled) and fast oscillating terms (where phase factors added). After the integration, oscillatory terms result in a much smaller contribution than slowly varying ones, and we can neglect them. This is usually referred to as rotating-wave approximation (RWA). Thus, taking into account only the signal contribution emitted into the phase-matched direction $\vec{k}_s=-\vec{k}_1+\vec{k}_2+\vec{k}_3$ under the RWA, one arrives at

$$\begin{aligned}P^{(3)}_{rw}(\tau,T,t)=&\exp[-i\omega_0 t+i\omega_0\tau]\int_0^\infty\int_0^\infty\int_0^\infty d\tau_a d\tau_b d\tau_c\\&\times\{S^{(3)}_{R,rw}(\tau_a,\tau_b,\tau_c)e^{-i\omega_0(\tau_c-\tau_a)}[\tilde{A}^*(t-t_1-\tau_a-\tau_b-\tau_c)\tilde{A}(t-t_2-\tau_b-\tau_c)\tilde{A}(t-t_3-\tau_c)\\&+\tilde{A}^*(t-t_1-\tau_a-\tau_b-\tau_c)\tilde{A}(t-t_3-\tau_b-\tau_c)\tilde{A}(t-t_2-\tau_c)]\\&+S^{(3)}_{NR,rw}(\tau_a,\tau_b,\tau_c)e^{i\omega_0(\tau_a+\tau_c)}[\tilde{A}(t-t_2-\tau_a-\tau_b-\tau_c)\tilde{A}^*(t-t_1-\tau_b-\tau_c)\tilde{A}(t-t_3-\tau_c)\\&+\tilde{A}(t-t_3-\tau_a-\tau_b-\tau_c)\tilde{A}^*(t-t_1-\tau_b-\tau_c)\tilde{A}(t-t_2-\tau_c)]\\&+S^{(3)}_{DC,rw}(\tau_a,\tau_b,\tau_c)e^{i\omega_0(\tau_a+2\tau_b+\tau_c)}[\tilde{A}(t-t_2-\tau_a-\tau_b-\tau_c)\tilde{A}(t-t_3-\tau_b-\tau_c)\tilde{A}^*(t-t_1-\tau_c)\\&+\tilde{A}(t-t_3-\tau_a-\tau_b-\tau_c)\tilde{A}(t-t_2-\tau_b-\tau_c)\tilde{A}^*(t-t_1-\tau_c)]\}.\end{aligned}\tag{4}$$

Herein the response functions $S^{(3)}_{R,rw}$, $S^{(3)}_{NR,rw}$, and $S^{(3)}_{DC,rw}$ are sums of Liouville pathways surviving the rotating-wave approximation, i.e., those which contain phase factors that approximately cancel with the corresponding electric field factors. We use t_1, t_2, and t_3 in Eq. (4) as an abbreviation for $-\tau-T$, $-T$, and 0 (compare Fig. 1) to elucidate that each $\tilde{A}$ represents an envelope of the first, second, or third pulse, respectively. The exponential factor in front of the integral indicates that the polarization oscillates at frequencies within a certain interval around $+\omega_0$ for the t coordinate and at frequencies within an interval around $-\omega_0$ for the τ coordinate. (This is the reason why the 2D spectra shown below, e.g., Fig. 6, have a negative ω_τ frequency axis and a positive ω_t frequency axis.) The integrand of Eq. (4) contains only slowly oscillating factors from the complex pulse envelopes. The details of the response functions S depend on the molecular system under study and will be given later in Sec. IV.

A two-dimensional Fourier transformation of $P^{(3)}_{rw}(\tau,T,t)$ with respect to τ and t then delivers two-dimensional (2D) spectra (one for each population time T) with frequency axes ω_τ and ω_t. However, experimentally one does not detect the polarization of Eq. (4) directly but rather the phase-matched signal field, which is in turn not observed as a function of t but instead with a spectrometer as a function of the conjugate frequency ω_t. Using Maxwell's equations, it can be seen that under ideal circumstances this frequency-domain signal field E_s is related to the polarization by

$$E_s(\tau,T,\omega_t)\sim\frac{i\omega_t}{n(\omega_t)}P^{(3)}(\tau,T,\omega_t)\tag{5}$$

with linear refractive index $n(\omega_t)$. Since one of the Fourier transformations is therefore already implicit in the frequency-domain detection technique, it is necessary to carry out only the transformation along the coherence time $\tau=t_2-t_1$ (for each fixed population time T), which finally leads to the 2D correlation spectra,

$$S_{2D}(\omega_\tau,T,\omega_t)=\int_{-\infty}^{\infty}iP^{(3)}(\tau,T,\omega_t)\exp(i\omega_\tau\tau)d\tau\tag{6}$$

for positive ω_t and negative ω_τ. The factor $iP^{(3)}(\tau,T,\omega_t)$ is easily obtained from the measured signal field via $E_s(\tau,T,\omega_t)n(\omega_t)/\omega_\tau$ and removes radiative line-shape distortions due to the factor of ω_t. In our experimental results we have ignored the frequency dependence of $n(\omega_t)$ as this is a very minor effect. For a very precise comparison of experiment and theory, pulse propagation effects can be taken into account by a suitable multidimensional frequency filter function.[22]

Note that the 2D spectra are complex-valued entities and therefore require separate plots of their real parts (''absorptive'' contribution) and imaginary parts (''refractive'' contribution), or alternatively, their absolute magnitude and phase. As can be seen from Eqs. (5) and (6), the (complex-valued) electric signal field has to be determined in both amplitude and phase in order to perform this Fourier-transform data analysis. Full characterization in our experiment will be done with the help of spectral interferometry. It should also be kept in mind that laser spectra have a finite width and therefore offer only a limited spectral ''window'' onto the frequency-domain nonlinear response function. It is hence preferable to implement 2D spectroscopy with a broadband and tunable light source such that the central laser wavelength can be matched to the relevant electronic transitions of the investigated system.

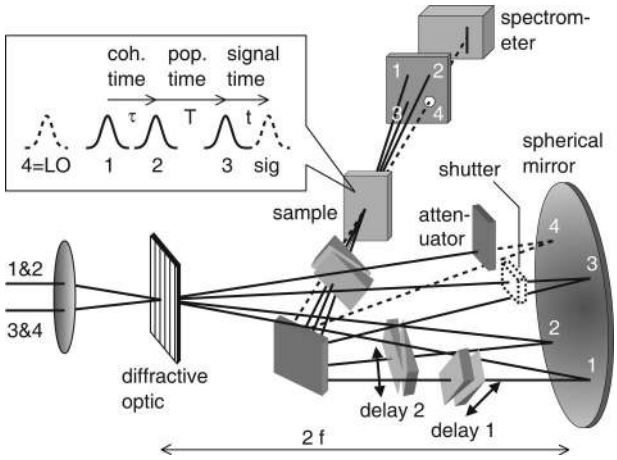

FIG. 2. Experimental setup. Two parallel beams of femtosecond laser pulses in the visible spectral region are focused by a lens onto a grating. The first diffraction orders emerge with high efficiency and provide the excitation pulses 1–3 as well as a local oscillator (4=LO) for heterodyne-detected three-pulse photon-echo electronic spectroscopy. A spherical mirror ($2f=50$ cm) creates an image of the pulse overlap in the sample cell via a plane folding mirror. The required time delays are provided with subwavelength precision by motor-controlled movable glass wedges. Full characterization of the nonlinear phase-matched signal field is carried out by spectral interferometry with the attenuated LO. An automated beam shutter is used for subtraction of scattering contributions. This diffractive-optics based setup is inherently phase-stabilized.

III. EXPERIMENT

A. Setup

One major difficulty in experimentally implementing 2D electronic spectroscopy is that, due to the phase factor in the Fourier kernel of Eq. (6), the coherence time needs to be varied with very high (interferometric) accuracy. Otherwise, artifacts can appear in the 2D traces after Fourier evaluation.[18] This is especially critical in the visible spectral region (as opposed to the infrared regime), because for shorter wavelengths a certain path-length fluctuation leads to a correspondingly higher phase error, and therefore the required accuracy is increasingly difficult to achieve. We have developed an inherently phase-stabilized setup to avoid this problem,[34] and recently Miller and coworkers have reported a similar technique.[35]

A home-built Ti:sapphire regenerative-amplifier laser system pumps a commercial OPA from Coherent to generate 30 μJ, 3 kHz laser pulses (attenuated for the experiment) between 400 nm and 700 nm (ca. 15 nm bandwidth). After passing a prism compressor, the pulses are split into two identical replicas, one of which is optionally delayed, before the two parallel and equal-intensity beams enter the experimental setup (Fig. 2). A 20 cm lens is used to create a common focus on a 30 grooves/mm diffractive optic (DO) which is optimized by design for highly efficient first-order diffraction. The emerging total number of four beams (positive and negative first orders, all others blocked by a mask) are then imaged by a spherical mirror at the distance of two focal lengths ($2f=50$ cm) via a plane folding mirror into a common spot within the sample cell. The focus diameter of 100 μm ($1/e^2$ intensity level as measured by the knife-edge method) is a good compromise between tight focusing (yielding larger signals), the necessity to illuminate enough grooves on the DO for good spatial separation of the diffracted beams, and the requirement to accommodate the delay-generating optical components.

Time delays for excitation pulses 1 and 2 are introduced with interferometric precision by means of movable glass wedges (thickness 1.5 mm, angle 1°, fused silica), addressed by computer-controlled stepper motors (Nanomover from Melles Griot). Each wedge is closely paired with an identical second one at antiparallel orientation. Lateral translation occurs along the inner surface, whereas the outer surfaces are aligned perpendicular to the laser beam. In this way, the beam is not displaced at all upon moving any of the wedges, and each pair effectively just acts as one glass plate of ''varying thickness.'' The dispersion introduced by the additional material is negligible but can also be compensated numerically if necessary, as will be shown in Sec. III B. Since the stepper motors are specified with 100 nm position repeatability, and a translation of 1 mm corresponds to a time delay of 27 fs, this leads to a nominal timing precision of 2.7 as over a total range of 400 fs. The calibration procedure is described in Sec. III B. For comparison, the time drift in previous 800 nm 2D spectroscopy was 0.1 fs over a time interval of 20 min, which was reduced to 40 as by the help of simultaneously recorded reference interferograms followed by numerical rephasing.[22] Note also that the use of the delay-generating wedges under normal incidence removes timing fluctuations that could originate from vibrations of the wedge holders, because to first order the glass path length does not change with fluctuations of the incidence angle. This is different if rotating glass slides under larger incidence angles are used to vary glass thickness and time delays.

The third beam also passes a wedge-pair combination,

which is used to balance the dispersion with respect to beams 1 and 2, and also to allow manual fine-tuning of its delay with respect to the local oscillator (LO) in beam 4. The computer-controlled shutter in beam 3 is used for automatic subtraction of unwanted scattering contributions as explained in Sec. III C. The LO is required for heterodyne detection of the signal field by spectral interferometry. It is attenuated by three to four orders of magnitude before it hits the sample. This ensures that it does not influence the response of the system. Furthermore the time ordering is such that the LO always arrives first. This guarantees (by causality) that the LO cannot be pump probe contaminated. But even if sufficient attenuation is not possible, the attenuator can be slightly tilted such that the resulting beam displacement moves the LO out of the pulse overlap in the sample cell. Then no mutual influences between excitation pulses or signal on the one hand and LO on the other hand are present at all, but the propagation of signal and LO after the sample is still sufficiently collinear to facilitate heterodyne detection.

Characterization of the third-order signal field is achieved by spectral interferometry with the local oscillator, which is positioned at time $t_{LO}=t_4\approx -700$ fs before pulse 3. Due to the phase-matching box geometry chosen here, the signal copropagates with the LO after the sample and is focused into a multichannel spectrometer (while the three excitation pulses are blocked by an aperture). This leads to spectral interference patterns

$$I_{SI}(\omega_t)=|E_s(\omega_t)+E_4(\omega_t)\exp[i\omega_t t_4]|^2, \tag{7}$$

where $E_s(\omega_t)$ is given by Eq. (5), and $E_4(\omega_t)$ is the LO field for delay $t_4=0$. Interferences are recorded with a 0.3 m imaging spectrograph and a 16 bit, 256×1024 pixel, thermoelectrically cooled charge-coupled device detector. For any given coherence time τ and population time T, a different spectrum is obtained [even though these parameters have been omitted from Eq. (7) for brevity]. Evaluation by a Fourier-transform method then yields the desired spectral signal intensity and phase (Sec. III C).

The major advantage of the DO-based setup is its inherent (i.e., passive) phase stability which can be understood in the following way. Imagine that there are fluctuations in the optical path lengths for each of the pulses 1–4 which lead to shifts Δt_i in the arrival times at the sample. Replacing t_i in Eq. (2) by $t_i+\Delta t_i$, the polarization from Eq. (4), and therefore also the signal field from Eq. (5), gets multiplied by $\exp[i\omega_0(-\Delta t_1+\Delta t_2+\Delta t_3)]$. This is easily seen by considering the phase factor $\exp[i\omega_0\tau]$ in front of the integral (and keeping in mind that we set $t_3=0$), whereas the little shifts within the slowly varying envelopes $\tilde{A}$ can be ignored because the Δt_i are assumed to be small. A similar time shift Δt_4 in beam 4 may affect the local oscillator, so that Eq. (7) is changed into

$$I_{SI}(\omega_t)=|E_s(\omega_t)\exp[i\omega_0(-\Delta t_1+\Delta t_2+\Delta t_3)] + E_4(\omega_t)\exp[i\omega_t t_4+i\omega_0\Delta t_4]|^2. \tag{8}$$

The measured signal will hence not be modified (i.e., the setup will be phase stabilized) if

$$-\Delta t_1+\Delta t_2+\Delta t_3-\Delta t_4=0. \tag{9}$$

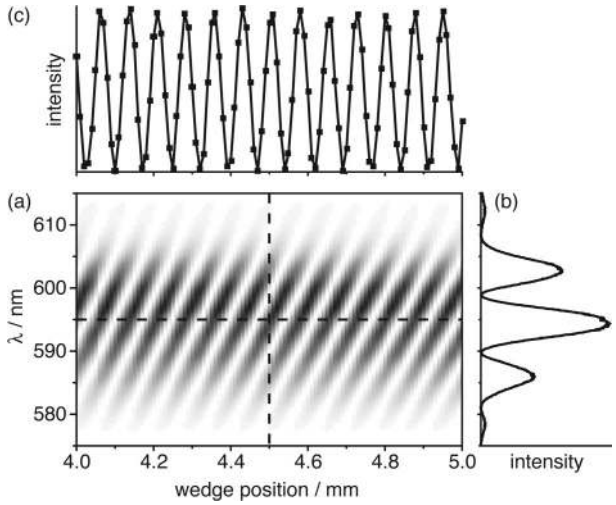

FIG. 3. Delay calibration by spectral interferometry. (a) Spectral interference patterns between pulses 1 and 2 are recorded in 10 μm steps by moving the glass wedge in arm 1. The cross section along the vertical dashed line shows (b) the spectral interference outside of the temporal pulse overlap, whereas the cross section along the horizontal dashed line delivers (c) the temporal oscillation for one particular wavelength. Counting these oscillations gives a precise calibration factor of wedge position vs time delay.

Consider now vibrations of the spherical mirror or the folding mirror as sources of path-length fluctuations. For a tilt of either mirror around its horizontal axis, for example, both Δt_1 and Δt_2 will change by the same amount and therefore cancel each other in Eq. (9). The same is true for Δt_3 and Δt_4. If the mirrors tilt around a vertical axis, then both Δt_1 and Δt_3 (or Δt_2 and Δt_4) change by the same amount, and again the net result is a cancellation. Since arbitrary vibrations are just linear combinations of these two examples, the total setup is inherently phase stabilized. Remaining phase instabilities are due to fluctuations which affect the four arms independently, e.g., air currents. This effect is reduced by the compact setup which guarantees almost uniform environmental conditions everywhere and which employs only one common mirror for the beam steering of all pulses. The DO setup is additionally enclosed in a suitable box.

B. Delay calibration

Even with phase stability, the introduction of time delays still needs to be done with subwavelength accuracy and linearity to facilitate Fourier evaluation without artifacts. This cannot be achieved easily by conventional delay stages because first, they would not fit into the DO-based setup (and at least the coherence-time delay has to be introduced after the splitting of the beams), and second, it would be very hard to obtain the required delay precision. The glass wedges, however, work like a ''gear transmission'' so that moderately precise mechanical movements are transferred into very precise time delays.

For the calibration procedure, the sample cell is replaced by another DO identical to the first one (alternatively, a simple pinhole can be used). This leads to diffraction of beam 1 and beam 2 into one common direction. Spectral interferograms similar to Eq. (7), but for identical pulses, are then recorded in 10 μm steps. The result is shown in Fig.

3(a). The temporal separation between adjacent interference maxima (along the horizontal wedge-position axis) depends on the wavelength (i.e., the vertical axis). For larger wavelengths, these separations are also larger and hence the interference plot shows ellipsoidal patterns which tilt the more the further the two laser pulses are separated in time. At the precise pulse overlap, one of the ellipses is exactly vertical. This fact is used to determine the time-delay zero point with interferometric precision. For a specific delay time outside of the pulse overlap, spectral interference is observed as in the cross section along the dashed line shown in Fig. 3(b). The cross-section for one particular wavelength, shown in Fig. 3(c) for the central wavelength of 595 nm, gives temporal oscillations which are present both within and outside of the temporal pulse overlap due to the spectral resolution. Since the measured wavelengths are known, "counting" the temporal oscillations delivers the conversion of wedge position into time delay. We use a sliding-window fast-Fourier transformation (FFT) to determine this calibration factor as a function of the wedge position. Hence, systematic variations in the glass thickness can be compensated for. However, since the relative standard deviation of the calibration factor in our case was only 10^{-4}, a single calibration constant was used (but determined separately for each one of the wedges).

One issue that needs to be addressed in this context is the additional material dispersion introduced by inserting more glass into the beam path. The dispersive spectral phase after an optical element of length l is

$$\Phi_d(\omega)=n(\omega)\omega l/c. \tag{10}$$

Consider now a Taylor expansion around the central laser frequency ω_0. The first-order Taylor coefficient introduces the desired time delay

$$\tau=\left.\frac{d\Phi}{d\omega}\right|_{\omega_0}=l\left[\frac{n-1}{c}+\frac{\omega}{c}\frac{dn}{d\omega}\right]_{\omega_0} \tag{11}$$

with respect to propagation in vacuum, whereas the second-order coefficient

$$b_2=\left.\frac{d^2\Phi}{d\omega^2}\right|_{\omega_0}=l\left[\frac{2}{c}\frac{dn}{d\omega}+\frac{\omega}{c}\frac{d^2n}{d\omega^2}\right]_{\omega_0} \tag{12}$$

is responsible for dispersion. Substituting for l in Eq. (12) from Eq. (11), one arrives at

$$b_2=\tau\left.\frac{2n'+\omega n''}{n-1+\omega n''}\right|_{\omega_0}, \tag{13}$$

and with specific values for fused silica[38] at $b_2=\tau\times 0.034$ fs.

The maximum delay introduced for the coherence period τ during the scans is 300 fs, such that the maximal dispersion coefficient is $b_2=10$ fs^2. At an initial pulse duration of $\tau_p=40$ fs, this leads to a broadening by a factor of only 1.6×10^{-4} and therefore can be neglected in its influence on the temporal amplitude envelopes. Hence, the response-function contributions to the time-domain convolution integral in Eq. (4) are unchanged. In principle, the additional dispersive phase $\Phi_d(\omega)$ is however transferred directly onto the signal phase $\Phi_s(\omega)$. This can be compensated numerically for each coherence time τ by using

$$\Phi_{s,\mathrm{corr}}(\omega)=\Phi_{s,\mathrm{meas}}(\omega)+\frac{b_2/\tau}{2}\tau(\omega-\omega_0)^2, \tag{14}$$

where $b_2/\tau=0.034$ fs is taken from Eq. (13) and the plus sign is obtained after careful analysis for the pulse order in Fig. 1, assuming balanced phases for $\tau=0$. Two-dimensional spectra calculated with this compensation procedure lead to results indistinguishable from those reported in Figs. 6 and 7 for our experimental parameters. However, in the case of much shorter pulses (and therefore broader bandwidth) the application of Eq. (14) may be useful.

Population times larger than zero are realized by reducing the glass thickness in both of the arms 1 and 2 by the same amount. This also leads to diminished dispersion for both pulses. However, these contributions cancel each other as they enter with opposite sign into Eq. (4), and hence Eq. (14) is still correct. Alternatively, population times larger than those conveniently realized by moving the glass wedges can be introduced with the conventional delay stage in front of the DO setup, by varying the delay for the pulse pair 1 and 2 at once. This time delay does not need to be introduced with subwavelength precision, because according to Eq. (4) the population time T enters only in the slowly varying envelopes and not into the critical phase factor in front of the integral. (All phase factors remaining within the integral cancel under the RWA and are completely independent of the pulse-center times or their fluctuations.) Hence also path-length fluctuations in the "conventional" part of the setup are not critical.

C. Data acquisition and evaluation

For any given population time T, the coherence time τ is scanned by moving pulse 1 from $-(\tau+T)$ to $-T$, and then moving pulse 2 from $-T$ to $-(\tau+T)$, typically in time steps of 2 fs. At each position, the electric signal field is determined by spectral interferometry. This part of the data analysis procedure is described in detail elsewhere.[17,39,40] Briefly, the spectral interferogram from Eq. (7) is Fourier transformed and a window applied which keeps only heterodyne contributions around time t_s-t_4 (with the LO arrival time $t_4\approx-700$ fs and the average signal time $t_s\gtrsim0$). After transformation back to the frequency domain, one obtains

$$I_f(\omega_t)=\sqrt{I_s(\omega_t)I_4(\omega_t)}\,\exp\{i[\Phi_s(\omega_t)-\Phi_4(\omega_t)-\omega_t t_4]\}, \tag{15}$$

from which both the desired signal intensity $I_s(\omega_t)$ and phase $\Phi_s(\omega_t)$ can be recovered. For this purpose, the LO spectrum $I_4(\omega_t)$ is determined at the beginning of the experiment such that it can be divided out. Since in our experimental configuration the LO also propagates through the sample cell, its phase may be subject to dispersion. This effect can be measured in a separate experiment by spectral interferometry, and the phase correction $\Phi_4(\omega_t)$ can be applied.

The overall shape of all the pulses 1–4 entering into the experiment is determined by second-harmonic generation

frequency-resolved optical gating (SHG-FROG) (Ref. 41) at the sample position with a 30 μm β-barium borate (BBO) crystal. Quantitative analysis in our case revealed near-transform-limited pulses of duration $\tau_p = 41$ fs at 595 nm (bandwidth product 0.57). To a good approximation, this input phase does not affect the measured 2D spectra (if the temporal pulse shape is not significantly altered) because all phases enter the spectral interference with mutually canceling signs, just as in the discussion of phase stability in Sec. III A. Hence the input phase was not included in the data analysis.[20] The determination of the LO delay t_4, which is needed in Eq. (15) as well, is described after Eq. (18) below. In principle, the signal intensity $I_s(\omega_t)$ could also be measured directly in homodyne detection by blocking beam 4. However, the application of heterodyne detection and Eq. (15) offers the advantage of "boosting" weak signals which would otherwise lie below the noise floor. In fact, we have achieved signal-to-noise ratios of 10^5 in the Fourier analysis, and for very weak signals we successfully performed 2D spectroscopy even when the maximum signal energy was below 100 aJ. This is possible because the phase stability allows realizing long CCD integration times without shifts in the spectral fringe patterns.

Application of Eqs. (5) and (6), i.e., Fourier transformation of the recovered signal field along the coherence time τ, finally leads to the desired 2D spectra. However, the presence of scattering in the sample cell can degrade the 2D signal quality due to unwanted light contributions propagating in the direction of the phase-matched signal. We show in the following how this problem can be solved by subtracting appropriate "noise" measurements.

In general, the spectrometer which is placed in beam 4 will detect a superposition of the electric fields from the local oscillator E_4, the third-order signal E_s, but also scattered light contributions E_1, E_2, and E_3 from the three excitation pulses which may furthermore be pump probe contaminated. In the notation used below, $E_\alpha \equiv [I_\alpha(\omega)]^{1/2} \exp[i\Phi_\alpha(\omega) + i\omega t_\alpha]$ contains the intensity and phase information as well as the average "arrival" time t_α for each of the contributions. The measured spectral intensity I_{1234} when all four incoming beams are present is then not given by Eq. (7) but rather by

$$I_{1234} = |E_1 + E_2 + E_3 + E_4 + E_s|^2 \tag{16}$$

$$\begin{aligned} &= (E_1+E_2)^* E_3 + (E_1+E_2)E_3^* + |E_1+E_2|^2 + |E_s|^2 \\ &\quad + (E_1+E_2)^* E_s + (E_1+E_2)E_s^* + E_3^* E_s + E_3 E_s^* \\ &\quad + (E_1+E_2)^* E_4 + (E_1+E_2)E_4^* + |E_3+E_4|^2 \\ &\quad + E_4^* E_s + E_4 E_s^* . \end{aligned} \tag{17}$$

In the ideal case, we would only want the terms from the last line, as they contain the desired information about the signal heterodyned with the local oscillator [compare with Eq. (15), where the second of these heterodyne terms has been removed by the Fourier windowing of the spectral-interferometry analysis]. And while all other terms also contribute to the raw data, only those terms survive the Fourier windowing as well which occur at approximately the same time difference of $t_s - t_4$ as the "true" signal. Since the local oscillator always comes first in time and never overlaps with any of the excitation pulses, the only surviving scattering terms are therefore those collected in the second-last line of Eq. (17), i.e., those at which the excitation pulses may overlap with the nonlinear signal and therefore appear at the same time difference with respect to the LO.

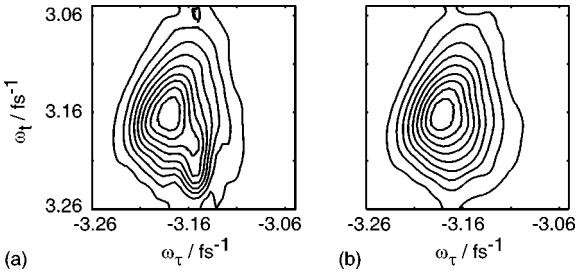

FIG. 4. Subtraction of undesired scattering. The absolute magnitude of a 2D spectrum for Nile Blue in acetonitrile at $T = 0$ fs is shown for a heavily scattering sample. (a) Without compensation, artifacts lead to a distortion of the contour lines. (b) Employing the correction method described in Sec. III C, these undesired effects disappear.

At the beginning of an experiment, we therefore record a scattering contribution where only pulses 3 and 4 are present,

$$I_{34} = |E_3 + E_4|^2, \tag{18}$$

which takes care of one of the undesired terms. Since the time separation between pulse 3 and 4 remains constant during 2D scans, the corresponding fringe pattern (18) is invariant and needs to be measured only once. Fourier evaluation of this term furthermore gives the LO delay time t_4 needed in the spectral-interferometry analysis of Eq. (15). The other undesired scattering terms are determined with beam paths 1, 2, and 4 opened

$$I_{124} = |E_1 + E_2 + E_4|^2 \tag{19}$$

$$= (E_1+E_2)^* E_4 + (E_1+E_2)E_4^* + |E_1+E_2|^2 + |E_4|^2 . \tag{20}$$

Since the time delays of pulses 1 and 2 are constantly varied, this spectrum has to be recorded for each time step separately, which is achieved by help of the automated shutter in beam 3 as indicated in Fig. 2.

During data analysis, the scattering-corrected spectra $I_{1234} - I_{34} - I_{124}$ are used for Fourier evaluation, which at times $\approx t_s - t_4$ only contain the desired heterodyne term $E_4^* E_s$. We have tested this procedure experimentally with a very strongly scattering sample (where the scattering was emphasized by picking a "bad spot" on the sample cell). Without scattering compensation, the resulting 2D trace [Fig. 4(a)] shows significant distortions even in the absolute-magnitude plot. However, with the procedure outlined above, these artifacts disappear [Fig. 4(b)]. This is especially useful for the investigation of molecular aggregates and biological samples with imperfect solubility properties. Note that this subtraction scheme exploits the phase relation between the signal heterodyne term and the scattering terms, which is well fulfilled in the inherently stabilized setup but might not work as well for conventional heterodyne schemes.

D. Phasing

The final step in the data analysis is the determination of the absolute phase of the 2D spectra. For this purpose, the projection-slice theorem is used which relates the real part of the projection of the 2D spectrum onto the ω_t axis with separately measurable spectrally resolved pump-probe data.[20,22] This separate measurement is carried out in the same experimental setup. Here it is necessary to record very small pump-probe effects in the visible spectral region (where the requirement for optical parametric amplifiers may lead to additional instabilities). Since conventional lock-in detection cannot be used because of the long CCD-detector integration time, we remove intensity fluctuations of the laser by recording reference laser spectra $I^{\mathrm{ref}}(\omega)$ simultaneously to the probe spectra $I^{\mathrm{pr}}(\omega)$, using a separate line on the CCD. Both types of spectrum are furthermore recorded both when the pump beam is present, $I_{\mathrm{pu}}(\omega)$, and when it is blocked, $I_0(\omega)$. This is achieved by a computer-controlled shutter in the pump beam.

For comparison between the results from 2D spectroscopy and pump probe, we then first calculate

$$A_{pp}(T,\omega)=\left(\frac{I_{\mathrm{pu}}^{\mathrm{pr}}(\omega)}{I_{\mathrm{pu}}^{\mathrm{ref}}(\omega)}-\frac{I_0^{\mathrm{pr}}(\omega)}{I_0^{\mathrm{ref}}(\omega)}\right)\frac{I_{\mathrm{pu}}^{\mathrm{ref}}(\omega)+I_0^{\mathrm{ref}}(\omega)}{2\sqrt{I_0^{\mathrm{pr}}(\omega)}} \qquad (21)$$

at pump-probe delay T. This determines the transient changes in the spectral nonlinear signal amplitude which is heterodyned with the probe field. The division of the first two terms by their respective reference intensities (recorded at the same time) ensures that the sensitive difference signal is not affected by laser noise. Since this division modifies the shape of the spectra, the difference signal is then again multiplied by the average of the two references (here the fluctuations are not critical because no difference is taken). Since we are ultimately interested in the signal field, we finally again divide by the probe field $[I_0^{\mathrm{pr}}(\omega)]^{1/2}$. The transient signal is alternatively obtained as a projection of the 2D spectrum

$$A_{2\mathrm{D}}(T,\omega_t)=\mathrm{Re}\left\{\frac{\omega_t}{n(\omega_t)}\int_{-\infty}^{\infty}S_{2\mathrm{D}}(\omega_\tau,T,\omega_t)\times\exp[i\Phi_c+i(\omega_t-\omega_0)t_c]d\omega_\tau\right\}, \qquad (22)$$

which should give the same shape (note that here the probe electric field is also not included). The 2D spectrum is multiplied by an overall constant phase correction Φ_c and a timing correction t_c which are varied such that the two plots using Eqs. (21) and (22) overlap. This procedure is called "phasing" and removes uncertainties in the interferometric phase relation Φ_4 of the LO with respect to pulse 3 and of its arrival time t_4, respectively.

Experimental results for Nile Blue are shown in Fig. 5. The open circles are the result from the pump-probe data $A_{pp}(T=0,\omega)$, and the solid line is the real part of the 2D projection $A_{2\mathrm{D}}(T=0,\omega_t)$ obtained from the data of Fig. 6 after suitable phasing. It is seen that the two data sets nicely overlap. We found that the value for the LO time t_4 obtained by evaluation of Eq. (18) always gave the best fit immediately, i.e., we obtained $t_c=0$. Because of the inherent phase stability of the setup, the same phase-correction values can be used for all population times.

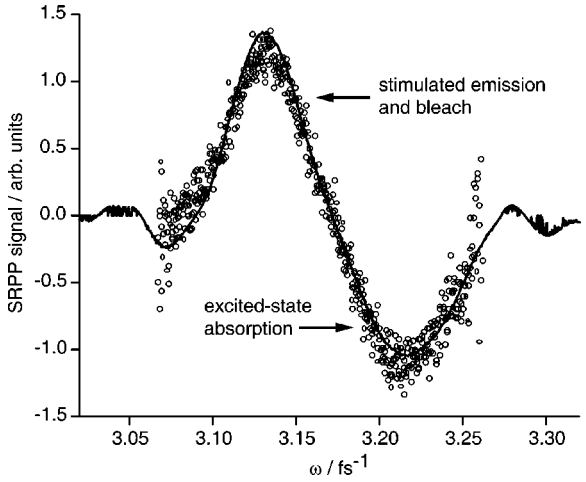

FIG. 5. Phasing of 2D spectra. The 2D-trace projection $A_{2\mathrm{D}}(T=0,\omega_t)$ is shown as the solid line whereas the open circles are obtained from spectrally resolved pump-probe measurements $A_{pp}(T=0,\omega)$. Positive signals correspond to increased light intensity (e.g., due to stimulated emission and ground-state bleach), whereas negative signals are mainly attributed to excited-state absorption. The good correspondence is a sign for the correct absolute phase of the 2D spectra, allowing to divide them into real and imaginary part as in Figs. 6 and 7.

In discussing Fig. 5, a positive contribution ("more light") is seen for smaller frequencies, and an almost equally strong negative contribution ("reduced light") for larger frequencies. These can be interpreted as mainly arising from stimulated emission and bleach versus excited-state absorption, respectively. The presence of excited-state absorption points at a third electronic level in this example, requiring an extension of the two-level response-function formalism. This is the topic of the following section. However, that description is also useful for other systems, because we are ultimately interested in tunable broadband 2D electronic spectroscopy, where in general more than two electronic levels will need to be considered.

IV. THEORY

To simulate the experimental results we have calculated the third-order nonlinear optical response for two- and three-electronic-level systems. While the treatment of a second excited state is common in infrared experiments,[42] higher excited electronic levels are often ignored in standard formulations of response-function calculations. We assume the electronic ground state $|g\rangle$, first excited state $|e\rangle$, and second excited state $|f\rangle$ to have energies ϵ_g, ϵ_e, and ϵ_f, and the nuclear degrees of freedom (DOF) in these states to be described by Hamiltonians $W_g(Q)$, $W_e(Q)$, and $W_f(Q)$, respectively. Here, Q is a collective coordinate of the nuclear DOF describing both the intramolecular vibrations and the influence of the solvent. For the frequency and bandwidth of the laser field we apply to the system, only the transitions $|g\rangle\rightarrow|e\rangle$ and $|e\rangle\rightarrow|f\rangle$ are relevant. Transition frequencies are defined as $\hbar\omega_{\alpha\beta}=\epsilon_\alpha-\epsilon_\beta$. We assume the Condon approximation to be valid, which allows usage of the vibra-

tional coordinate-independent dipole-moment operator. Thus, the complete Hamiltonian of the molecular system and laser field reads

$$H = H_S - VE(t) \tag{23}$$

with the molecular Hamiltonian

$$H_S = \sum_{\alpha=g,e,f} \{\epsilon_\alpha + W_\alpha(Q)\}|\alpha\rangle\langle\alpha|, \tag{24}$$

and

$$V = d_{eg}|e\rangle\langle g| + d_{fe}|f\rangle\langle e| + \text{c.c.}, \tag{25}$$

where the dipole matrix elements of the two electronic transitions are given by d_{eg} and d_{fe}.

To calculate the third-order nonlinear response of the system, which is responsible for the photon echo signal, we employ the standard perturbation theory and RWA as described in Ref. 1 and Sec. II. Since in our sample molecule Nile Blue the width of the absorption spectrum is small compared to the center transition frequency, we also expect deviations from the RWA to be small.[43] For the three-level system, the response functions from Eq. (4) will read as follows: The "rephasing" contribution $S^{(3)}_{R,rw}$ includes only Liouville pathways with approximate oscillatory factor $e^{i\omega_0(\tau_c-\tau_a)}$, i.e., those which contribute to the creation of an echo signal. As is shown in the Appendix, it can be written as the sum of three terms:

$$S^{(3)}_{R,rw}(\tau_a,\tau_b,\tau_c) = R_{2g}(\tau_a,\tau_b,\tau_c) + R_{3g}(\tau_a,\tau_b,\tau_c) - R^*_{1f}(\tau_a,\tau_b,\tau_c). \tag{26}$$

Similarly, the "nonrephasing" part

$$S^{(3)}_{NR,rw}(\tau_a,\tau_b,\tau_c) = R_{1g}(\tau_a,\tau_b,\tau_c) + R_{4g}(\tau_a,\tau_b,\tau_c) - R^*_{2f}(\tau_a,\tau_b,\tau_c) \tag{27}$$

includes only pathways that oscillate with $\approx e^{-i\omega_0(\tau_a+\tau_c)}$, i.e., those which contribute only as a free-induction decay. And finally, the "double coherence" contribution oscillates with $e^{-i\omega_0(\tau_a+2\tau_b+\tau_c)}$ and reads

$$S^{(3)}_{DC,rw}(\tau_a,\tau_b,\tau_c) = R_{4f}(\tau_a,\tau_b,\tau_c) - R^*_{3f}(\tau_a,\tau_b,\tau_c). \tag{28}$$

Using the results of the Appendix, we can express the different pathways in terms of four line-shape functions

$$g_{\alpha\beta}(t) = \int_0^t d\tau_1 \int_0^{\tau_1} d\tau_2 \langle \delta\omega_{\alpha g}(\tau_2)\,\delta\omega_{\beta g}(0)\rangle, \quad \alpha,\beta = e,f \tag{29}$$

with

$$\delta\omega_{\alpha g}(t) = \frac{1}{\hbar} U_g^\dagger(t)[W_\alpha(Q) - W_g(Q)]U_g(t). \tag{30}$$

The ground-state evolution operator $U_g(t)$ is defined as

$$U_g(t) = \exp\left\{-\frac{i}{\hbar} W_g(Q)t\right\}. \tag{31}$$

For pathways including ground and first excited states only, we obtain standard expressions which can be found in Ref. 1 and transformed into the current notation by substitutions $g(t) \equiv g_{ee}(t)$ and $R_n \equiv R_{ng}$ where $n = 1,\ldots,4$. However, the pathways involving the second excited state read

$$\begin{aligned} R_{1f}(\tau_a,\tau_b,\tau_c) = {} & |d_{eg}|^2|d_{fe}|^2 e^{-i\omega_{eg}\tau_c + i\omega_{fe}\tau_a} \\ & \times \exp\{-g^*_{ee}(\tau_b) - g^*_{ff}(\tau_a) \\ & - g_{ee}(\tau_a+\tau_b+\tau_c) + g^*_{ef}(\tau_b) - g^*_{ef}(\tau_a+\tau_b) \\ & + g^*_{ef}(\tau_a) - g^*_{ee}(\tau_a+\tau_b) + g^*_{ee}(\tau_a) \\ & - g_{ee}(\tau_c) \quad + g_{ee}(\tau_b+\tau_c) + g^*_{fe}(\tau_a) \\ & - g_{fe}(\tau_b+\tau_c) \quad - g_{fe}(\tau_a+\tau_b+\tau_c)\}, \end{aligned} \tag{32}$$

$$\begin{aligned} R_{2f}(\tau_a,\tau_b,\tau_c) = {} & |d_{eg}|^2|d_{fe}|^2 e^{i\omega_{eg}\tau_c + i\omega_{fe}\tau_a} \\ & \times \exp\{-g^*_{ee}(\tau_b+\tau_c) - g^*_{ff}(\tau_a) \\ & - g_{ee}(\tau_a+\tau_b) + g^*_{ef}(\tau_b+\tau_c) \\ & - g^*_{ef}(\tau_a+\tau_b+\tau_c) + g^*_{ef}(\tau_a) \\ & - g^*_{ee}(\tau_a+\tau_b+\tau_c) + g^*_{ee}(\tau_a) - g^*_{ee}(\tau_c) \\ & + g_{ee}(\tau_b) + g^*_{fe}(\tau_a) - g_{fe}(\tau_b) \\ & - g_{fe}(\tau_a+\tau_b)\}, \end{aligned} \tag{33}$$

$$\begin{aligned} R_{3f}(\tau_a,\tau_b,\tau_c) = {} & |d_{eg}|^2|d_{fe}|^2 e^{i\omega_{eg}(\tau_b+\tau_c) + i\omega_{fe}(\tau_a+\tau_b)} \\ & \times \exp\{-g^*_{ee}(\tau_c) - g^*_{ff}(\tau_a+\tau_b) - g_{ee}(\tau_a) \\ & + g^*_{ef}(\tau_c) - g^*_{ef}(\tau_a+\tau_b+\tau_c) + g^*_{ef}(\tau_a+\tau_b) \\ & - g^*_{ee}(\tau_a+\tau_b+\tau_c) + g^*_{ee}(\tau_a+\tau_b) \\ & - g^*_{ee}(\tau_b+\tau_c) + g^*_{ee}(\tau_b) + g^*_{fe}(\tau_a+\tau_b) \\ & - g^*_{fe}(\tau_b) - g_{fe}(\tau_a)\}, \end{aligned} \tag{34}$$

$$\begin{aligned} R_{4f}(\tau_a,\tau_b,\tau_c) = {} & |d_{eg}|^2|d_{fe}|^2 e^{-i\omega_{eg}(\tau_a+\tau_b+\tau_c) - i\omega_{fe}\tau_b} \\ & \times \exp\{-g_{ee}(\tau_a) - g_{ff}(\tau_b) - g_{ee}(\tau_c) \\ & + g_{ef}(\tau_a) - g_{ef}(\tau_a+\tau_b) + g_{ef}(\tau_b) \\ & - g_{ee}(\tau_a+\tau_b) + g_{ee}(\tau_b) \\ & - g_{ee}(\tau_a+\tau_b+\tau_c) + g_{ee}(\tau_b+\tau_c) \\ & + g_{fe}(\tau_b) - g_{fe}(\tau_b+\tau_c) - g_{fe}(\tau_c)\}. \end{aligned} \tag{35}$$

The third-order nonlinear optical response function, which is related to the signal generated by Eq. (4), is fully determined by the four line-shape functions $g_{ee}(t)$, $g_{ef}(t)$, $g_{fe}(t)$, and $g_{ff}(t)$, the system transition frequencies ω_{eg} and ω_{fe}, and the transition dipole moments d_{eg} and d_{fe}. In fact, for a conventional echo peak-shift measurement, just the ratio of the dipole moments d_{fe}/d_{eg} is significant, since only the position of the integrated echo maximum is measured.

As it is indicated in Eq. (29), the form of the line-shape function $g_{\alpha\beta}(t)$ depends on the corresponding energy-gap correlation functions

$$C_{\alpha\beta}(t) = \hbar^2 \langle \delta\omega_{\alpha g}(t)\,\delta\omega_{\beta g}(0)\rangle. \tag{36}$$

The terms $C_{ee}(t)$ and $C_{ff}(t)$ correlate the energy-gap function with itself and are related to their respective spectral densities by a Fourier transformation as described in Ref. 1.

Introducing the spectral density $\rho(\omega)$, one can rewrite Eq. (29) into a more convenient form. Thus, we define

$$\omega^2\rho(\omega)=C''(\omega), \tag{37}$$

where $C''(\omega)$ is the Fourier transformation of the imaginary part of the energy-gap correlation function $C(t)$ (we dropped indices for brevity). Using the spectral density, we define the reorganization energy

$$\lambda=\frac{1}{\pi}\int_0^\infty \omega\rho(\omega)d\omega \tag{38}$$

as well as two normalized $[M'(t=0)=M''(t=0)=1]$ real functions

$$M'(t)=\frac{1}{\pi\Delta^2}\int_0^\infty \omega^2\rho(\omega)\coth(\beta\hbar\omega/2)\cos(\omega t)d\omega, \tag{39}$$

$$M''(t)=\frac{1}{\pi\lambda}\int_0^\infty \omega\rho(\omega)\cos(\omega t)d\omega, \tag{40}$$

where β is the usual Boltzmann inverse temperature factor, and we recast Eq. (29) into (we omit indices again)

$$g(t)=\Delta^2\int_0^t d\tau_1\int_0^{\tau_1} d\tau_2 M'(\tau_2)-i\lambda\int_0^t d\tau[1-M''(\tau)]. \tag{41}$$

Here $\Delta^2=(1/\pi)\int_0^\infty\omega^2\rho(\omega)\coth(\beta\hbar\omega/2)d\omega$. Since $M''(t)$ and $\rho(\omega)$ in Eq. (40) are related by a cosine Fourier transformation (CFT), we can write $\omega\rho(\omega)=\lambda\mathrm{CFT}^{-1}[M''(t)](\omega)$, where CFT^{-1} denotes inverse cosine Fourier transformation. Thus, $g(t)$ can be calculated from a given $M''(t)$ which prescribes its shape by postulating a single parameter λ and temperature. Usually, one assumes $g(t)$ of a real system to be a compound of several components of different origins, e.g., inertial solvent motion, intramolecular vibrations, etc. Each component is characterized by its own characteristic shape $M''(t)$ and its reorganization energy λ. Thus, for the total density of states we have

$$\omega\rho(\omega)=\sum_c \lambda_c\mathrm{CFT}^{-1}[M_c''(t)](\omega). \tag{42}$$

For the "off-diagonal" correlation functions $C_{ef}(t)$ and $C_{fe}(t)$ we can perform a similar analysis to that one presented above, leading in general to slightly different relations between the Fourier transformations of their real and imaginary parts. It is not obvious what should be the actual form of these functions in terms of usual *ansatz* forms used for the "diagonal" correlation functions. However, assuming $C_{ef}(t)=C_{fe}(t)$, the frequency-domain symmetries appear to be the same as in the diagonal case and we therefore will use the same functional forms for both diagonal and off-diagonal line-shape functions throughout this work, with different parameters to account for their differences. The comparison of the simulations with the experimental data may indicate if such an approach is indeed sufficient.

In previous work on Nile Blue,[44] peak-shift measurements have been successfully explained using $g(t)$ consisting of two simple solvent modes and a vibrational contribution including 40 intramolecular vibrational modes taken from the resonance Raman measurements by Mathies and co-workers.[45] In this work we use the vibrational part $g_{vib}(t)$ of the total $g(t)$ with the same definition and parameters as in Ref. 44. The solvent part of the line-shape function is modeled by a Gaussian and an exponential mode with their $M''(t)$ functions defined as

$$M_g''(t)=\exp\left[-\left(\frac{t}{\tau_g}\right)^2\right], \tag{43}$$

$$M_e''(t)=\exp\left[-\frac{t}{\tau_e}\right], \tag{44}$$

and reorganization energies λ_g and λ_e, respectively. The fast Gaussian component is usually attributed to the inertial motion of the solvent and a slower exponential solvation component models diffusional and structural relaxation of the solvent. The total $g(t)$ of the system will be considered to be a sum of the solvent and vibrational contributions

$$g(t)=g_{solv}(t)+g_{vib}(t). \tag{45}$$

V. RESULTS AND DISCUSSION

A. Experiment

In order to illustrate the feasibility of tunable two-dimensional spectroscopy in the visible, we carried out measurements on the dye molecule Nile Blue in acetonitrile at a center wavelength of 595 nm. This prototype system had already been investigated with conventional three-pulse photon-echo peak-shift (3PEPS) spectroscopy in earlier work,[44,46] where primarily the influence of intramolecular vibrations was discussed. For the 2D spectroscopy, we followed the data acquisition and analysis procedure of Sec. III to obtain electronic correlation spectra for a number of different population times between $T=0$ fs and $T=100$ fs.

The results are plotted in Figs. 6 and 7. We point out that these relatively large numbers of 2D traces for different population times are easily obtained with the phase-stabilized setup because interferometric stability is routinely maintained over total measurement times of around 10 h. The real parts of the 2D traces can be roughly interpreted as the transient field amplitude at a particular "probe frequency" ω_t, induced by a specific "excitation frequency" ω_τ and after the waiting time T. In this sense, it can be understood as spectrally resolved transient absorption where in addition the pump pulse is also spectrally resolved. It should be kept in mind, however, that different Liouville pathways contribute to this signal which are not limited to excited-state population evolution alone. The imaginary part correspondingly describes refractive index variations at certain frequencies ω_t, induced by excitation at ω_τ. The diagonal inclination of the real part at early population times indicates disorder which is consistent with the observation of a peak-shift signal in 3PEPS spectroscopy. This diagonal shape mainly means that the emission frequency ω_t is correlated with the excitation frequency ω_τ, i.e., the molecule "remembers" the initial excitation.

However, as the population time T is increased, the 2D spectra get more and more symmetric around the vertical

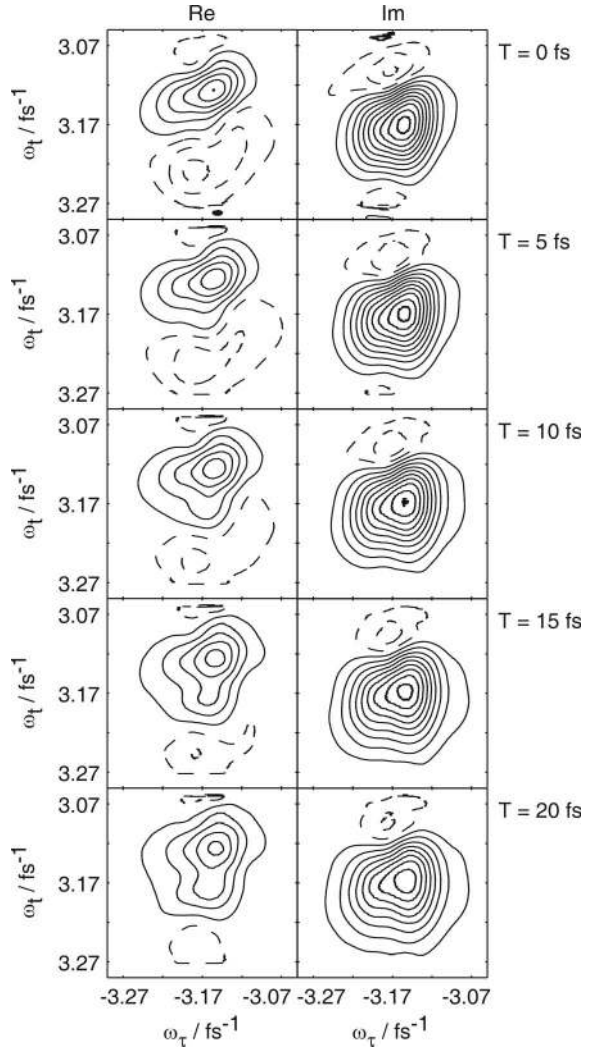

FIG. 6. Experimental 2D spectra for Nile Blue in acetonitrile. Each spectrum is an average over three individual scans for that particular population time. Because of the stability of the setup, the background amplitude levels outside the shown regions are below 2% of the peak values. Contour lines are drawn in 10% intervals at $-95\%,-85\%,\ldots,-5\%,5\%,\ldots,95\%$ for the absorptive real parts (left column) and refractive imaginary parts (right column) of $S_{2D}(\omega_\tau,T,\omega_t)$. The level of 100% is determined from the highest peak value within the series, here occurring for the imaginary part at $T=0$ fs. Solid contour lines correspond to positive and dashed lines to negative amplitudes. In this evaluation, the dispersion of the LO was not compensated, thus yielding the signal phase at the entrance rather than the exit of the sample cuvette.

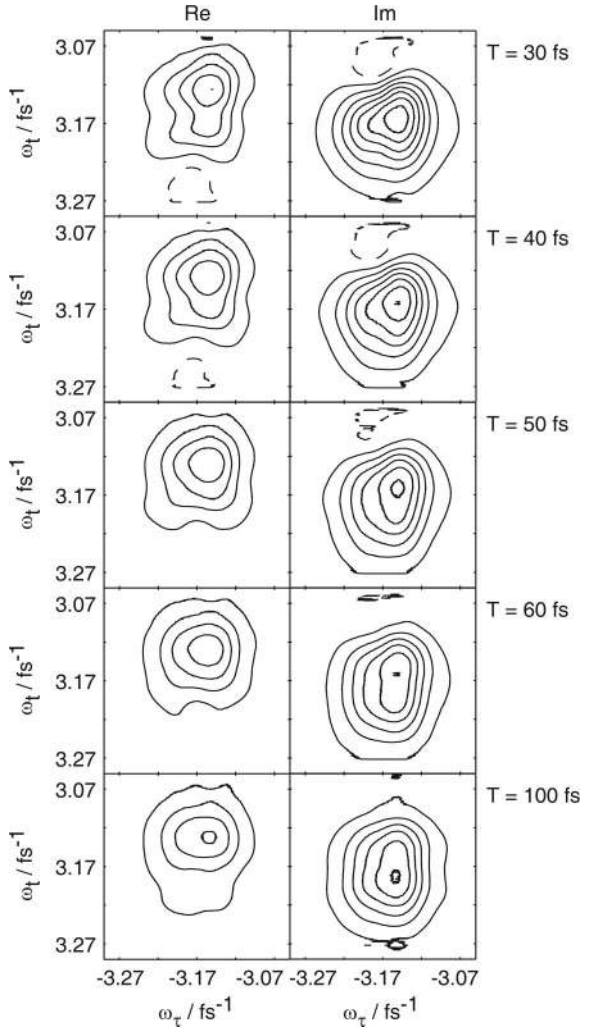

FIG. 7. Experimental 2D spectra for Nile Blue. This data set is the continuation of Fig. 6 for larger population times.

axis, and the correlation (i.e., memory) of the initial excitation is lost. Furthermore, the region of negative signal in the 2D real part disappears. The same trend of increasing symmetry and loss of correlation with larger population times can be observed in the imaginary 2D part, and the absolute scale of the signal (both Re and Im) gets smaller. At 100 fs, no further change in the 2D spectra can be observed. This behavior is consistent with the decay of the 3PEPS on the same time scale.[44,46]

B. Simulation

In this part we simulate experimental results using the two- and three-electronic-level model. In particular, we want to clarify the origin of the main features in the experimental 2D trace. Of central interest are here the negative features in both the real and imaginary part of the 2D spectrum. The real part of the experimental 2D trace in Figs. 6 and 7 is mostly positive for long populations times T, but shows significant negative features for short T. A previous study using a two-level model[19] suggested that the negative features can be produced by a simultaneous creation of coherent wave packets in the ground and excited states.

Thus, as a reference we calculated 2D spectra using the two-level model. In Fig. 8 the 2D traces for population times $T=0$ fs and $T=100$ fs are presented for different line-shape functions $g_{ee}(t)$ and different durations of the laser pulses. In Figs. 8(a) and 8(b) a simple line-shape function is assumed, including one Gaussian mode with $\tau_g=60$ fs and reorganization energy $\lambda_g=140$ cm^{-1}. Since the negative features in the experimental 2D traces disappear on the time scale of the FWHM of the laser pulses, we first study the influence of the laser pulse length on the 2D spectrum. In Fig. 8(a), a δ pulse is applied, and due to its infinite spectral width we obtain broad spectral features. Clearly some negative features appear. Also the symmetrization of the spectra for larger population times T is very pronounced. However, the imaginary part shows a large negative feature even at long times, and

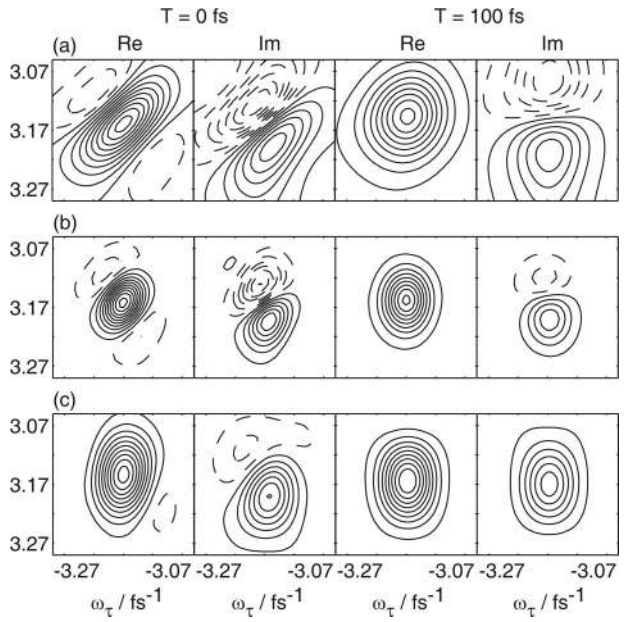

FIG. 8. Theoretical 2D spectra for a two-level system. (a) The system is characterized by a line-shape function $g_{ee}(t)$ resulting from a correlation function $M(t)$ of a simple Gaussian form with $\tau_g = 60$ fs and reorganization energy $\lambda_g = 140$ cm^{-1}, subject to δ-pulse excitation. Population times $T = 0$ fs and $T = 100$ fs are presented. The laser frequency matches the maximum of the absorption spectrum. (b) The same molecular parameters are used as in part (a), only the laser pulse duration is equal to 41 fs. (c) The system is characterized by a line-shape function $g_{ee}(t)$ correctly reproducing the linear absorption spectrum (see description in the text) and the same laser frequency detuning with respect to the absorption maximum and pulse length as in the experiment.

also the slope and relative intensity of positive and negative features is different from the experiment. Using the experimental FWHM pulse duration of 41 fs in Fig. 8(b) does not change the picture significantly. The spectral features become smaller in extension due to the limited spectral window covered by the laser pulse.[19]

Although reproducing main features of the 2D traces, this simple form of the line-shape function $g_{ee}(t)$ cannot be accepted as a candidate for the qualitative explanation of 2D spectra of Nile Blue, because it does not correctly reproduce the linear absorption spectrum and 3PEPS measurements. Also the ratio of the intensities of real versus imaginary parts of the 2D spectrum is in favor of the real part, whereas the experimental traces show the opposite tendency.

Previously,[44,46] both linear spectrum and 3PEPS of Nile Blue were successfully accounted for. In addition to Gaussian and exponential solvent modes, 40 vibrational modes of intramolecular DOF were included, with parameters obtained from resonance Raman experiments.[45] In Fig. 8(c) we use the $g_{ee}(t)$ of Ref. 44 including all these modes and the correct experimental laser frequency detuning with respect to the absorption maximum of the linear spectrum. It is immediately seen that the presence of the intramolecular modes results in a reduction of the negative features in both the real and imaginary part of the spectrum. Most significantly, the negative feature in the imaginary part disappears for long times in accordance with the experimental observation. On the other hand, this model still does not correctly reproduce the relatively higher intensity of the imaginary part of the 2D trace with respect to the real one, and especially the negative feature in the real part at $T = 0$ is much too small as compared to experiment.

The pump-probe measurement (see Fig. 5) suggests the presence of a higher excited state in Nile Blue, and consequently its influence on the 2D spectrum has to be discussed. The linear absorption spectrum of Nile Blue shows several excited states in the vicinity of $\omega_{fg} = \omega_{fe} + \omega_{eg}$ with $\omega_{fe} \approx \omega_{eg}$. In the following discussion, we will therefore accept the hypothesis that an optical transition from the first excited state of Nile Blue ($|e\rangle$ in our notation) into some of these higher excited states or into another state invisible in the linear spectrum is allowed. Simulating the three-level-system optical response is significantly more complicated than the two-level response due to the presence of additional line-shape functions $g_{ef}(t)$ and $g_{ff}(t)$. While the $g_{ee}(t)$ line-shape function is bound to correctly explain the linear spectrum and the same can be said about $g_{ff}(t)$ if the participating higher excited state were known, no such restriction is put on $g_{ef}(t)$. As discussed above, $g_{ef}(t)$ arises from the corresponding correlation function $C_{ef}(t)$ which describes correlations between energy gaps of the $|g\rangle \rightarrow |e\rangle$ and $|g\rangle \rightarrow |f\rangle$ transitions. Very little *a priori* can be said about the form of this function. However, as will be seen below, the 2D traces are sensitive to $g_{ef}(t)$, and therefore we can use 2D spectroscopy as a tool to learn about excited-state correlations, i.e., about electronic coherences in solution-phase photoprocesses.

For the current purposes, we will assume $g_{ff}(t) = g_{ee}(t)$ and study the limiting cases of $g_{ef}(t) = 0$ and $g_{ef}(t) = g_{ee}(t)$ to obtain insight into the influence of the different parameters. Thus in Fig. 9 we study the influence of the second excited state $|f\rangle$ on the 2D spectrum. We start again with a simple $g_{ee}(t)$ with one solvent mode and the second excited state. In Fig. 9(a) we investigate the three-level model with the second transition frequency $\omega_{fe} = \omega_{eg} + 100$ cm^{-1} and the ratio of dipole moments $d_{fe}/d_{eg} = 1$. The line-shape function $g_{ef}(t)$ is set to zero. Comparing with the corresponding two-level results of Fig. 8(b) and the experimental results of Fig. 6 we can see encouraging changes toward the reproduction of the experimental features. For $T = 0$ the "lower" negative feature in the real part is now stronger, and a new negative feature appears in the lower section of the imaginary part. With increasing T the lower negative feature in the real part of the 2D spectrum moves from its rather "diagonal" position to the "vertical" one in a parallel manner to the experiment. The detailed evolution with T (not shown) indicates that this feature becomes weaker until about $T = 30$ fs, but later regains intensity. In the experimental trace, the feature disappears completely. Comparison of Figs. 8(b) and 9(a) also reveals that the ratio of the real and imaginary part intensities is closer to the experiment in the three-level model than in the two-level one. Furthermore, the relative intensities depend on the relative strength of both electronic transition dipole moments as will be demonstrated below.

Employing the second limiting case $g_{ef}(t) = g_{ee}(t)$ reveals that the "disappearance" of the long-living negative

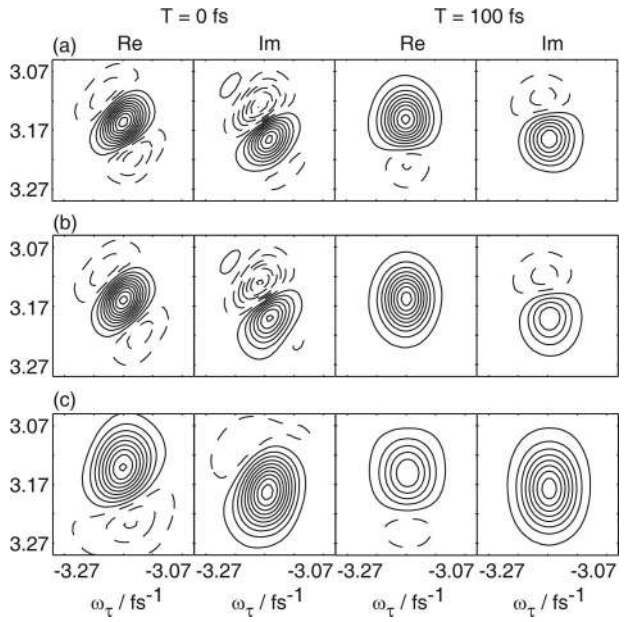

FIG. 9. Theoretical 2D spectra for a three-level system. (a) The line-shape functions $g_{ee}(t)=g_{ff}(t)$ result from a correlation function $M(t)$ of a simple Gaussian form with $\tau_g=60$ fs and reorganization energy $\lambda_g=140$ cm^{-1}, and $g_{ef}(t)=0$. The second transition frequency is $\omega_{fe}=\omega_{eg}+100$ cm^{-1}. The laser frequency matches the absorption maximum of the linear absorption spectrum and the pulse length is 41 fs. (b) The same parameters are used as in part (a), only $g_{ef}(t)=g_{ee}(t)=g_{ff}(t)$. (c) The line-shape function $g_{ee}(t)=g_{ff}(t)$ is used that correctly reproduces the linear absorption spectrum (see description in the text) and the same laser frequency detuning with respect to the absorption maximum, and the same pulse length as in the experiment. In this case we set $g_{ef}(t)=0$. All figure parts are obtained with ratios $d_{fe}/d_{eg}=1$.

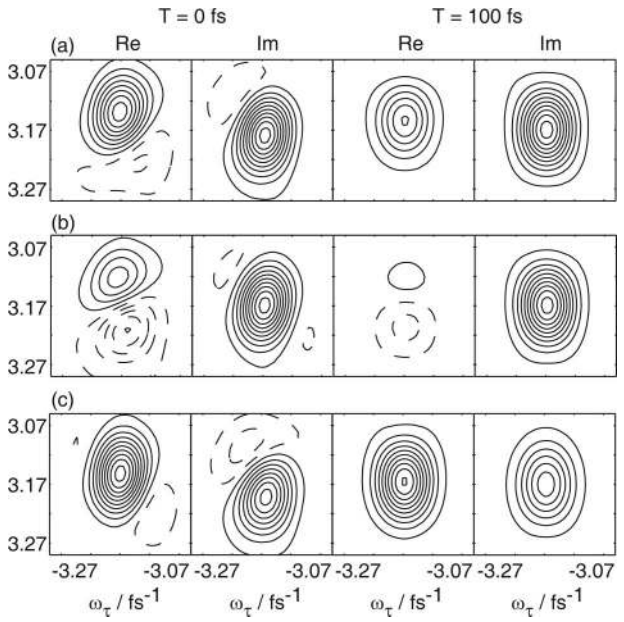

FIG. 10. Influence of dipole strength and $g_{ef}(t)$ parameters in the three-level system. (a) The same line-shape functions are used as in Fig. 9(a), but with $\omega_{fe}=\omega_{eg}$, the laser detuning is as in the experiment, $g_{ef}(t)=0$, and $d_{fe}/d_{eg}=1$. (b) The same parameters are employed as in part (a), only $d_{fe}/d_{eg}=1.5$. (c) The same parameters are used as in part (b), only $g_{ef}(t)=g_{ee}(t)$.

feature in the real part of the 2D spectrum is controlled by the $g_{ef}(t)$ function. The correlation between the two energy gaps disables the excited-state absorption for longer T as it can be seen in Fig. 9(b). Indeed, for $T=100$ fs the two-level [Fig. 8(b)] and three-level results [Fig. 9(b)] become almost identical when $g_{ef}(t)=g_{ee}(t)$.

Figure 9(c) presents the 2D traces for the same parameters as in Fig. 9(a) [i.e., $g_{ef}(t)=0$], but now again with $g_{ee}(t)=g_{ff}(t)$ including all modes from Ref. 44. In this case the experimental 2D traces are qualitatively well reproduced, especially at shorter times. The correct shape and intensity of the negative features in the real and imaginary part are obtained, and also the reduction of the peak amplitudes with larger times is seen as in the experiment. Furthermore, the imaginary part of the spectrum is now stronger than the corresponding real part in accordance with experiment. However, due to the fact that $g_{ef}(t)=0$, the negative feature in the real part survives to long times which is not the case experimentally.

If we set $g_{ef}(t)=g_{ee}(t)$ in the case of all vibrational modes (not shown), the same conclusion as obtained from Fig. 9(b) can be drawn, i.e., the negative feature in the imaginary part disappears for long times and the results are very similar to those already seen for two levels [Fig. 8(c)].

Looking at the experimental 2D traces one can therefore conclude that they indeed exhibit signatures of a second excited level. Interestingly, the 2D spectrum is sensitive to the correlation between the two excited levels, and the experimental trace suggests that $g_{ef}(t)$ is nonzero (otherwise the negative features in the real part would survive to long times T). This means we have available a method to determine electronic coherences between excited states. In the molecule here, these correlations constitute an intermediate case between the two limits $g_{ef}(t)=0$ and $g_{ef}(t)=g_{ee}(t)$. A more detailed determination of the form of $g_{ef}(t)$ requires further investigation which is in progress.

In Fig. 10 we further study the influence of the dipole-moment strength ratio d_{fe}/d_{eg} on the 2D spectrum using the complete-mode $g(t)$ functions from Ref. 44. Figure 10(a) shows the three-level results for $d_{fe}/d_{eg}=1$, $g_{ef}(t)=0$ and $\omega_{fe}=\omega_{eg}$. Here the two electronic transitions are on the same frequency and thus the negative feature which would otherwise be surviving in the real part of the 2D spectrum is covered by a large positive one. If we increase the ratio to $d_{fe}/d_{eg}=1.5$ [Fig. 10(b)], the negative features exceed the positive ones. Comparing Figs. 10(a) and 10(b) demonstrates that the imaginary part remains mostly untouched by increasing the dipole ratio, but the real part is very sensitive. Thus, the dipole ratio could be assessed from the 2D measurement in the case of uncorrelated excited levels. As Fig. 10(c) reveals (still for $d_{fe}/d_{eg}=1.5$), the presence of the coherence [again $g_{ef}(t)=g_{ee}(t)$] influences the 2D spectrum significantly.

VI. CONCLUSION

In this paper we have described the technique, application, and analysis of phase-stabilized two-dimensional (2D) spectroscopy for electronic transitions. Following the pioneering work of Jonas and coworkers,[17–22] we can now record low-noise 2D Fourier-transform spectra throughout

the visible wavelength region, using broadband tunable light sources (optical parametric amplifiers). This is due to the very compact diffractive-optic-based setup, which furthermore employs only two beam-steering elements common to all excitation beams and the local oscillator.[34] The introduction of highly accurate delay times with better than λ/100 precision and repeatability removes experimental artifacts that can be present when conventional delay stages are used. Together with automated subtraction of unwanted scattering terms, the 2D background is below 2%. The stability also facilitates very high sensitivity (<100 aJ signal energy) because long CCD integration times can be realized without loss of heterodyne fringe contrast. All of this makes our approach very suitable for investigating biological samples or other excitonically coupled systems where high excitation intensities have to be avoided. While the technique has been applied here in the visible spectral range (where stability issues are more critical), similar setups should also be of benefit in 2D infrared spectroscopy.

The understanding of the features of 2D spectra of relatively simple dye molecules such as Nile Blue represents an important prerequisite to a successful interpretation of more complicated 2D spectra of complex systems with coupled chromophores. The simulations performed in this paper reveal considerable sensitivity of the method to the correlation properties of the electronic states involved in the 2D spectrum. In particular we found that to explain the experimental data on Nile Blue, a three-level model has to be employed. This will also be necessary in general for 2D spectroscopy with broadband excitation, because more and more transition frequencies can be covered. The 2D spectroscopy is sensitive to the correlation between the two excited levels, and the degree of correlation between them controls the disappearance of the features attributed to the excited-state absorption. We have studied the two extreme cases of a strict correlation between excited states and complete absence of their correlation and found the line-shape function $g_{ef}(t)$ of Nile Blue in acetonitrile to fall somewhere in between these two cases. The precise form of the $g_{ef}(t)$ line-shape function can, in principle, be obtained by careful fitting of the experimental 2D spectra including their dependence on the population time T. A simple picture of the correlation function $C_{ef}(t)$ leading to $g_{ef}(t)$ is the following: If level $|e\rangle$ fluctuates in energy by a certain amount, $C_{ef}(t=0)$ tells us to what degree level $|f\rangle$ shifts into the same direction and by the same amount, and $C_{ef}(t>0)$ indicates if this correlated shift also persists for longer times.

Future prospects of 2D visible spectroscopy include the direct measurement of electronic coupling. An investigation of an excitonically coupled system (J aggregate) with 2D spectroscopy will be presented elsewhere.[47] We expect 2D electronic spectroscopy to be of great value also in biological systems such as light-harvesting complexes. Valuable insights could be obtained by analyzing both the intensities and shapes of diagonal peaks as well as those of "cross peaks." This can lead to direct two-dimensional frequency "maps" of electronic couplings.

ACKNOWLEDGMENTS

We thank Mino Yang for an initial version of the two-level response-function code and helpful discussions. We also thank Minhaeng Cho for valuable discussions. This work was supported by a grant from the NSF. T.B. thanks the German Science Foundation (DFG) for an Emmy-Noether Fellowship.

APPENDIX A: THIRD-ORDER RESPONSE FUNCTION FOR THREE-LEVEL SYSTEMS

For a general N-level system in interaction with the electric field of a laser, the third-order response function $S^{(3)}(\tau_a,\tau_b,\tau_c)$ can be written in terms of Liouville pathways as[1]

$$S^{(3)}(\tau_a,\tau_b,\tau_c)=\left(\frac{i}{\hbar}\right)^3\Theta(\tau_a)\Theta(\tau_b)\Theta(\tau_c)\times\sum_{\alpha=1}^{4}[R_\alpha(\tau_a,\tau_b,\tau_c)-R_\alpha^*(\tau_a,\tau_b,\tau_c)], \tag{A1}$$

where

$$R_1(\tau_a,\tau_b,\tau_c)=\mathrm{Tr}\{V(\tau_a)V(\tau_a+\tau_b)V(\tau_a+\tau_b+\tau_c)\times V(0)\rho(-\infty)\}, \tag{A2}$$

$$R_2(\tau_a,\tau_b,\tau_c)=\mathrm{Tr}\{V(0)V(\tau_a+\tau_b)V(\tau_a+\tau_b+\tau_c)\times V(\tau_a)\rho(-\infty)\}, \tag{A3}$$

$$R_3(\tau_a,\tau_b,\tau_c)=\mathrm{Tr}\{V(0)V(\tau_a)V(\tau_a+\tau_b+\tau_c)\times V(\tau_a+\tau_b)\rho(-\infty)\}, \tag{A4}$$

$$R_4(\tau_a,\tau_b,\tau_c)=\mathrm{Tr}\{V(\tau_a+\tau_b+\tau_c)V(\tau_a+\tau_b)V(\tau_a)\times V(0)\rho(-\infty)\}. \tag{A5}$$

Here,

$$V(t)=e^{i/\hbar H_S t}Ve^{-i/\hbar H_S t} \tag{A6}$$

is the dipole-moment operator in interaction representation, with system Hamiltonian H_S. The concrete form of the expressions (A2)–(A5) depends on the properties of the dipole operator V.

In our three-level system, the electronic dipole-moment operator can be represented by a 3×3 matrix

$$V=\begin{pmatrix}0 & d_{eg} & 0\\ d_{eg}^* & 0 & d_{fe}\\ 0 & d_{fe}^* & 0\end{pmatrix}. \tag{A7}$$

In this case, all of the pathways split into two contributions, one that recovers the standard two-level pathway expression and one involving the second excited state. Thus we can write

$$S^{(3)}(\tau_a,\tau_b,\tau_c)=\left(\frac{i}{\hbar}\right)^3\Theta(\tau_a)\Theta(\tau_b)\Theta(\tau_c)\times\sum_{\alpha=1}^{4}\sum_{\beta=g,f}[R_{\alpha\beta}(\tau_a,\tau_b,\tau_c)-R^*_{\alpha\beta}(\tau_a,\tau_b,\tau_c)], \quad \text{(A8)}$$

where the additional index β equals g for two-level pathways (leading through the $|g\rangle$ and $|e\rangle$ states only), and $\beta=f$ for the ones that have third-level contributions (leading through the second excited state $|f\rangle$), respectively. The pathways can be written in terms of two functions F_β, $\beta=g,f$ as

$$R_{1\beta}(\tau_a,\tau_b,\tau_c)=F_\beta(\tau_a,\tau_a+\tau_b,\tau_a+\tau_b+\tau_c,0), \quad \text{(A9)}$$

$$R_{2\beta}(\tau_a,\tau_b,\tau_c)=F_\beta(0,\tau_a+\tau_b,\tau_a+\tau_b+\tau_c,\tau_a), \quad \text{(A10)}$$

$$R_{3\beta}(\tau_a,\tau_b,\tau_c)=F_\beta(0,\tau_a,\tau_a+\tau_b+\tau_c,\tau_a+\tau_b), \quad \text{(A11)}$$

$$R_{4\beta}(\tau_a,\tau_b,\tau_c)=F_\beta(\tau_a+\tau_b+\tau_c,\tau_a+\tau_b,\tau_a,0), \quad \text{(A12)}$$

where

$$F_\beta(\tau_1,\tau_2,\tau_3,\tau_4)=|d_{eg}|^2|d_{\beta e}|^2\mathrm{Tr}\{\mathcal{G}_{ge}(\tau_1)\mathcal{G}_{e\beta}(\tau_2)\mathcal{G}_{\beta e}(\tau_3)\times\mathcal{G}_{eg}(\tau_4)\rho(-\infty)\}. \quad \text{(A13)}$$

The $\mathcal{G}$'s are defined by time-ordered exponentials[1] as

$$\mathcal{G}_{ab}(t)=\exp_-\left\{\frac{i}{\hbar}\int_0^t\delta\omega_{ag}(\tau)d\tau\right\}\times\exp_+\left\{-\frac{i}{\hbar}\int_0^t\delta\omega_{bg}(\tau)d\tau\right\}, \quad \text{(A14)}$$

where $a,b=e,f$, and $\delta\omega_{ag}(t)$ has been defined in Sec. IV. In the case of $\mathcal{G}_{ab}(t)$ involving either a or b equal to g, the corresponding time-ordered exponential turns into the unity operator because $\delta\omega_{gg}=0$.

Introducing the cumulant expansion,[1] the F functions of Eq. (A13) can be expressed in terms of the line-shape functions defined by Eq. (29). It reads

$$F_\beta(\tau_1,\tau_2,\tau_3,\tau_4)=|d_{eg}|^2|d_{\beta e}|^2e^{i\omega_{eg}(\tau_1-\tau_4)+i\omega_{e\beta}(\tau_2-\tau_3)}\times\exp\{-h_\beta(\tau_1,\tau_2,\tau_3,\tau_4)\} \quad \text{(A15)}$$

with

$$\begin{aligned}h_f(\tau_1,\tau_2,\tau_3,\tau_4)&=g_{ee}(\tau_1-\tau_2)+g_{ff}(\tau_2-\tau_3)+g_{ee}(\tau_3-\tau_4)\\&\quad-g_{ef}(\tau_1-\tau_2)+g_{ef}(\tau_1-\tau_3)-g_{ef}(\tau_2-\tau_3)\\&\quad+g_{ee}(\tau_1-\tau_3)-g_{ee}(\tau_2-\tau_3)+g_{ee}(\tau_1-\tau_4)\\&\quad-g_{ee}(\tau_2-\tau_4)-g_{fe}(\tau_2-\tau_3)+g_{fe}(\tau_2-\tau_4)\\&\quad+g_{fe}(\tau_3-\tau_4),\end{aligned} \quad \text{(A16)}$$

and

$$\begin{aligned}h_g(\tau_1,\tau_2,\tau_3,\tau_4)&=g_{ee}(\tau_1-\tau_2)+g_{ee}(\tau_3-\tau_4)\\&\quad+g_{ee}(\tau_1-\tau_3)-g_{ee}(\tau_2-\tau_3)\\&\quad+g_{ee}(\tau_1-\tau_4)-g_{ee}(\tau_2-\tau_4).\end{aligned} \quad \text{(A17)}$$

The final expressions (26) and (27) are obtained after invoking the rotating-wave approximation (RWA) and assuming the outcoming signal in the direction $-\vec{k}_1+\vec{k}_2+\vec{k}_3$.

[1] S. Mukamel, *Principles of Nonlinear Optical Spectroscopy* (Oxford University Press, New York, 1995).
[2] S. Mukamel, Annu. Rev. Phys. Chem. **51**, 691 (2000).
[3] C. Scheurer and S. Mukamel, J. Chem. Phys. **115**, 4989 (2001).
[4] M. Cho, PhysChemComm **5**, 40 (2002).
[5] P. Hamm, M. Lim, and R. M. Hochstrasser, J. Phys. Chem. B **102**, 6123 (1998).
[6] S. Woutersen and P. Hamm, J. Phys. Chem. B **104**, 11316 (2000).
[7] M. C. Asplund, M. T. Zanni, and R. M. Hochstrasser, Proc. Natl. Acad. Sci. U.S.A. **96**, 8219 (2000).
[8] N.-H. Ge, M. T. Zanni, and R. M. Hochstrasser, J. Phys. Chem. A **106**, 962 (2002).
[9] C. Fang, J. Wang, A. K. Charnley, W. Barber-Armstrong, A. B. Smith III, S. M. Decatur, and R. M. Hochstrasser, Chem. Phys. Lett. **382**, 586 (2003).
[10] O. Golonzka, M. Khalil, N. Demirdöven, and A. Tokmakoff, Phys. Rev. Lett. **86**, 2154 (2001).
[11] N. Demirdöven, M. Khalil, and A. Tokmakoff, Phys. Rev. Lett. **89**, 237401 (2002).
[12] M. Khalil, N. Demirdöven, and A. Tokmakoff, Phys. Rev. Lett. **90**, 047401 (2003).
[13] L. Lepetit and M. Joffre, Opt. Lett. **21**, 564 (2002).
[14] J.-P. Likforman, M. Joffre, and V. Thierry-Mieg, Opt. Lett. **22**, 1104 (1997).
[15] N. Belabas and M. Joffre, Opt. Lett. **27**, 2043 (2002).
[16] M. F. Emde, W. P. de Boeij, M. S. Pshenichnikov, and D. A. Wiersma, Opt. Lett. **22**, 1338 (1997).
[17] S. M. Gallagher, A. W. Albrecht, T. D. Hybl, B. L. Landin, B. Rajaram, and D. M. Jonas, J. Opt. Soc. Am. B **15**, 2338 (1998).
[18] J. D. Hybl, A. W. Albrecht, S. M. Gallagher Faeder, and D. M. Jonas, Chem. Phys. Lett. **297**, 307 (1998).
[19] S. M. Gallagher Faeder and D. M. Jonas, J. Phys. Chem. A **103**, 10489 (1999).
[20] J. D. Hybl, A. Albrecht Ferro, and D. M. Jonas, J. Chem. Phys. **115**, 6606 (2001).
[21] J. D. Hybl, A. Yu, D. A. Farrow, and D. M. Jonas, J. Phys. Chem. A **106**, 7651 (2002).
[22] D. M. Jonas, Annu. Rev. Phys. Chem. **54**, 425 (2003).
[23] P. Tian, D. Keusters, Y. Suzaki, and W. S. Warren, Science **300**, 1553 (2003).
[24] M. Cho, N. F. Scherer, G. R. Fleming, and S. Mukamel, J. Chem. Phys. **96**, 5618 (1992).
[25] J.-Y. Bigot, M.-A. Mycek, S. Weiss, R. G. Ulbrich, and D. S. Chemla, Phys. Rev. Lett. **70**, 3307 (1993).
[26] W. P. de Boeij, M. S. Pshenichnikov, and D. A. Wiersma, Chem. Phys. Lett. **238**, 1 (1995).
[27] W. P. de Boeij, M. S. Pshenichnikov, and D. A. Wiersma, Chem. Phys. **233**, 287 (1998).
[28] A. A. Maznev, K. A. Nelson, and T. A. Rogers, Opt. Lett. **23**, 1319 (1998).
[29] G. D. Goodno, G. Dadusc, and R. J. D. Miller, J. Opt. Soc. Am. B **15**, 1791 (1998).
[30] G. D. Goodno, V. Astinov, and R. J. D. Miller, J. Phys. Chem. B **103**, 603 (1999).
[31] M. Khalil, N. Demirdöven, O. Golonzka, C. J. Fecko, and A. Tokmakoff, J. Phys. Chem. A **104**, 5711 (2000).
[32] Q.-H. Xu, Y.-Z. Ma, I. V. Stiopkin, and G. R. Fleming, J. Chem. Phys. **116**, 9333 (2002).
[33] J. P. Ogilvie, M. L. Cowan, M. Armstrong, A. Nagy, and R. J. D. Miller, *Ultrafast Phenomena XIII*, Springer Series in Chemical Physics Vol. 71, edited by R. J. D. Miller, M. M. Murnane, N. F. Scherer, and A. M. Weiner (Springer, Berlin, 2003), pp. 571–573.
[34] T. Brixner, I. V. Stiopkin, and G. R. Fleming, Opt. Lett. **29**, 884 (2004).

[35] M. L. Cowan, J. P. Ogilvie, and R. J. D. Miller, Chem. Phys. Lett. **386**, 184 (2004).
[36] A. W. Albrecht, J. D. Hybl, S. M. Gallagher Faeder, and D. M. Jonas, J. Chem. Phys. **111**, 10934 (1999).
[37] A. W. Albrecht Ferro, J. D. Hybl, S. M. Gallagher Faeder, and D. M. Jonas, J. Chem. Phys. **115**, 5691 (2001).
[38] J.-C. Diels and W. Rudolph, *Ultrashort Laser Pulse Phenomena* (Academic, San Diego, 1996).
[39] L. Lepetit, G. Chériaux, and M. Joffre, J. Opt. Soc. Am. B **12**, 2467 (1995).
[40] C. Dorrer, N. Belabas, J.-P. Likforman, and M. Joffre, J. Opt. Soc. Am. B **17**, 1795 (2000).
[41] R. Trebino, K. W. DeLong, D. N. Fittinghoff, J. N. Sweetser, M. A. Krumbügel, B. A. Richman, and D. J. Kane, Rev. Sci. Instrum. **68**, 3277 (1997).
[42] P. Hamm, M. Lim, and R. M. Hochstrasser, Phys. Rev. Lett. **81**, 5326 (1998).
[43] A. Albrecht Ferro, J. D. Hybl, and D. M. Jonas, J. Chem. Phys. **114**, 4649 (2001).
[44] K. Ohta, D. S. Larsen, M. Yang, and G. R. Fleming, J. Chem. Phys. **114**, 8020 (2001).
[45] M. K. Lawless and R. A. Mathies, J. Chem. Phys. **96**, 8037 (1992).
[46] D. S. Larsen, K. Ohta, Q.-H. Xu, M. Cyrier, and G. R. Fleming, J. Chem. Phys. **114**, 8008 (2001).
[47] I. Stiopkin, T. Brixner, and G. R. Fleming (unpublished).